

# Numerical Simulation of Bubbles under an Inclined Plane: Application to Aluminum Electrolysis<sup>1</sup>

Alexandre Caboussat<sup>a,2</sup>

<sup>a</sup>University of Houston, Department of Mathematics,  
4800 Calhoun Rd, Houston, Texas 77204 - 3008, USA  
caboussat@math.uh.edu

Jacques Rappaz<sup>b</sup>

<sup>b</sup>Mathematics Institute of Computational Science and Engineering  
Ecole Polytechnique Fédérale de Lausanne, 1015 Lausanne, Switzerland  
jacques.rappaz@epfl.ch

---

## Abstract

The numerical investigation of large bubbles rising under an inclined plane is presented. A numerical method for the simulation of fluid flows with complex free surfaces is presented, in which the liquid is assumed to be Newtonian, while gas bubbles are assumed to be compressible. A volume-of-fluid method is used to track the liquid domain. A time splitting algorithm allows to decouple the advection and diffusion operators, the compressibility effects in the gas, and the surface tension effects. Finite element techniques are coupled with a characteristics method with a two grids method. Numerical simulations are in excellent agreement with experimental data.

## Key words

Two-phases flow, Large bubbles, Volume-of-fluid formulation, Time splitting algorithm, Two-grids method, Aluminum electrolysis.

**2010 MSC:** 65M25, 65M60, 76D05, 76N15, 76T10

---

<sup>1</sup> Project supported by Rio Tinto - Alcan company.

<sup>2</sup> Supported by the Mathematics Institute of Computational Science and Engineering (EPFL-MATHICSE).

## 1 Introduction and Motivations

The industrial production of aluminum is based on the electrolysis process. In most countries, aluminum is produced from alumina ( $\text{Al}_2\text{O}_3$ ) which itself comes from bauxite. Aluminum electrolysis is performed in large *Hall-Héroult cells* (of approximate size 15 meters long times 3 meters wide times 1 meter high). Figure 1 visualizes a schematic representation of a vertical transverse cut of such a cell. Alumina particles are injected periodically in a corrosive electrolytic bath lying over the liquid aluminum. Both fluids are kept at temperature  $T = 965$  C and are immiscible.

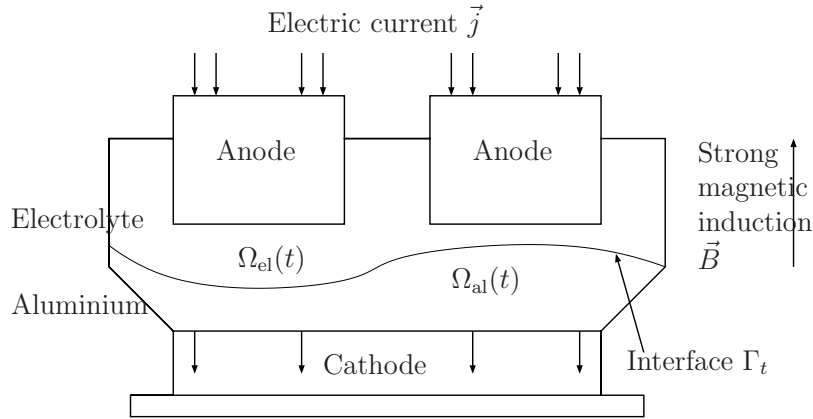
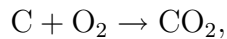


Fig. 1. Aluminum electrolysis cell: sketch and notation.

A strong electric current (whose density is about  $10'000 \text{ A/m}^2$ ) runs through the fluids from the carbon anodes to the cathode allowing electrolysis to take place in the electrolyte. The chemical reaction producing the liquid aluminum and the oxygen is the following:



It gradually burns the anode and creates  $\text{CO}_2$  gas bubbles under the anode:



which forces the anodes to be replaced periodically. Moreover, since the interface between both liquids is not flat, the bottom of the anodes are inclined and large bubbles of  $\text{CO}_2$  moving under the anode perturb the mechanism and performance of the cell. On the other hand, alumina is added regularly to the electrolytic bath, so that the aluminum is produced and gathered at the bottom of the cell. The aluminum industry wants to optimize the production by increasing the current density as much as possible, or by acting on the geometrical and electrical configurations of such electrolytic cells.

This coupled problem involves many physical phenomena, as there is a two-phases flow in the cell, with a free surface, together with electromagnetic and gravity forces. The motion of the interface between fluids has to be controlled to ensure the *stability* of the cell [6]. The Navier-Stokes equations in the two-phases flow are coupled with the Maxwell equations in the whole space for the computation of electromagnetic effects [7], resulting in complete *magnetohydrodynamics (MHD)* problem.

In this article, we focus on the movement of gas bubbles nucleated under the anodes during aluminum reduction. The understanding of the formation and movement of such bubbles is essential for a good control of the electrolysis process, as they play a significant role in the mass and momentum transfer in the cell, as well as the creation of electrically resistant zones: the bubble layer can indeed cover between 24 and 90 percent of the surface of the anode, and one-third of the height of the bath, which influences drastically the electromagnetic properties of the bath [18].

Experimental results [22, 23] have shown that not only the volume flow rate of the bubble nucleation, but also the size and the shape of the single bubbles are very important for the electrolysis process, especially when it comes to the influence of large bubbles (*Fortin bubbles* [8]) that transfer high amounts of momentum to the fluid and help to homogenize the temperature field and the mass transport in the bath.

In order to reproduce this phenomenon, we consider the case of a large bubble under an inclined plane [12, 15, 17]. For large bubbles, the surface tension effects are not predominant. Experiments show that large bubbles break up into smaller parts right before escaping from under the anode.

The purpose of this article is thus the simulation of large bubbles under an inclined plane and the comparison of numerical results with experiments in order to benchmark the numerical approach. In order to do so, we introduce a model for the behavior of gas ( $\text{CO}_2$ ) bubbles in the electrolyte bath (see Figure 1).

The numerical model is based on a time splitting approach [10] and a two-grids method. This allows advection and diffusion phenomena to be decoupled, as well as the treatment of the liquid and gas phases. Finite element techniques [9] are used to solve the diffusion phenomena using an unstructured mesh of the cavity containing the liquid. A forward characteristic method [19] on a structured grid allows advection phenomena to be solved efficiently.

The article is structured as follows. In Section 2, the model is presented: the liquid is an incompressible Newtonian fluid, the gas in the bubble is compressible, and surface tension effects are incorporated on the interface. A time

splitting scheme is described in Section 3, and a multi-grids method is presented in Section 4. Finally, results of simulations of large bubbles in two and three dimensions of spaces are presented in Sections 5 and 6 respectively, and compared with experimental results.

## 2 Modeling of Two-Phases Flow and Gas Bubbles

We describe here a mathematical model for the numerical simulation of liquid-gas free surface flow with surface tension effects on the liquid-gas interface. This model is inspired from [4, 5, 13, 14].

Let  $\Lambda$  be a cavity of  $\mathbb{R}^d$ ,  $d = 2, 3$  in which the fluid must be confined, and let  $T > 0$  be the final time of simulation. For any given time  $t$ , let  $\Omega_t$  be the domain occupied by the liquid and let  $\Gamma_t$  be the free surface defined by  $\partial\Omega_t \setminus \partial\Lambda$ . The notations are reported in Figure 2 in the frame of a two-dimensional situation, namely the rising of a bubble initially under an inclined plane, under gravity forces.

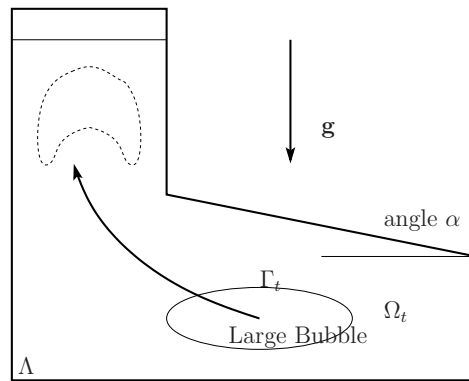


Fig. 2. Rising of a bubble of gas under gravity forces in a cavity  $\Lambda$  filled with water.

Let  $Q_T$  denote the space-time domain containing the liquid, that is  $Q_T = \{(x, t) : x \in \Omega_t, 0 < t < T\}$ . In the liquid region, the velocity field  $\mathbf{v} : Q_T \rightarrow \mathbb{R}^d$  and the pressure field  $p : Q_T \rightarrow \mathbb{R}$  are assumed to satisfy the time-dependent, incompressible Navier-Stokes equations, that is

$$\rho \frac{\partial \mathbf{v}}{\partial t} + \rho (\mathbf{v} \cdot \nabla) \mathbf{v} - 2 \nabla \cdot (\mu \mathbf{D}(\mathbf{v})) + \nabla p = \mathbf{f} \quad \text{in } Q_T, \quad (1)$$

$$\nabla \cdot \mathbf{v} = 0 \quad \text{in } Q_T. \quad (2)$$

Here  $\mathbf{D}(\mathbf{v}) = 1/2(\nabla \mathbf{v} + \nabla \mathbf{v}^T)$  is the rate of deformation tensor,  $\rho$  the constant density,  $\mu$  the viscosity and  $\mathbf{f}$  denotes the external forces.

Let  $\varphi : \Lambda \times (0, T) \rightarrow \mathbb{R}$  be the characteristic function of the liquid domain

$Q_T$ . The function  $\varphi$  equals one if liquid is present, zero if it is not. In order to describe the kinematics of the free surface,  $\varphi$  must satisfy (in a weak sense):

$$\frac{\partial \varphi}{\partial t} + \mathbf{v} \cdot \nabla \varphi = 0 \quad \text{in } \Lambda \times (0, T), \quad (3)$$

where  $\mathbf{v}$  outside  $Q_T$  is a continuous extension of  $\mathbf{v}$  inside  $Q_T$ . More precisely,  $\mathbf{v}(\mathbf{X}(t), t) = \mathbf{v}(\mathbf{X}(0), 0)$ , where  $\mathbf{X}(t)$  is the trajectory of a fluid particle, thus  $\mathbf{X}'(t) = \mathbf{v}(\mathbf{X}(t), t)$ .

In the gas region, the velocity is disregarded, so that the only unknown is the pressure. At each time  $t$ , the pressure  $P(t) : \Lambda \setminus \Omega_t \rightarrow \mathbb{R}$  in the gas is assumed to be piecewise constant in each bubble of gas, that is in each connected component of the gas domain. The gas is supposed to be an ideal gas at constant temperature. Let us denote by  $k(t)$  the total number of bubbles of gas at time  $t \in (0, T)$  and by  $B_i(t)$  the bubble number  $i$ . The law of ideal gases is assumed to hold in each bubble, which implies

$$P_i(t)V_i(t) = \text{constant in bubble number } i. \quad (4)$$

The velocity in the gas is thus disregarded and the connected components of the gas domain have to be tracked at each time step. In most situations and when the time step is small enough, three situations may appear between two time steps at different locations in the process:

- (i) a single bubble may remain a single bubble;
- (ii) a bubble may split into two bubbles;
- (iii) two bubbles may merge into one.

In these three cases, the pressure at time  $t + \tau$  may be computed by taking into account the conservation of number of molecules in the bubbles between the time  $t$  and  $t + \tau$ . A detailed discussion may be found in [5].

The initial conditions are the following. At initial time, the characteristic function of the liquid domain  $\varphi$  is given, which defines the initial liquid region  $\Omega_0 = \{x \in \Lambda : \varphi(x, 0) = 1\}$ . The initial velocity field  $\mathbf{v}$  is then prescribed in  $\Omega_0$ . The initial gas pressure field is prescribed in  $\Lambda \setminus \Omega_0$  and is assumed to be constant in each bubble of gas existing at initial time.

The boundary conditions for the velocity field are the following. On the boundary of the liquid region being in contact with the walls (that is to say the boundary of  $\Lambda$ , see Figure 2), Dirichlet, slip or Signorini boundary conditions are enforced, see [13, 14]. On the free surface  $\Gamma_t$ , we assume that the forces are the normal forces due to the gas pressure and the surface tension effects. At given time  $t$ , let  $\kappa(x, t)$  be the Gauss curvature of the interface  $\Gamma_t$  at point  $x$ . The following equilibrium relation is then satisfied on the liquid-gas interface:

$$-p\mathbf{n} + 2\mu\mathbf{D}(\mathbf{v})\mathbf{n} = -P\mathbf{n} + \sigma\kappa\mathbf{n} \quad \text{on } \Gamma_t, \quad t \in (0, T), \quad (5)$$

where  $\mathbf{n}$  is the unit normal of the liquid-gas free surface oriented toward the gas domain,  $P$  is the pressure in the gas,  $\kappa$  is the local curvature of the interface and  $\sigma$  is a constant surface tension coefficient which depends on both media on each side of the interface (namely the liquid and the gas).

For example, consider the situation of Figure 2: When the bubble rises, a force (5) is exerted on the interface; the first contribution of this force is a normal force induced by the pressure of the trapped gas which prevents the bubble from collapsing, while the second contribution is due to the surface tension effects.

The model unknowns are the characteristic function  $\varphi$  in the whole cavity, the velocity  $\mathbf{v}$  and pressure  $p$  in the liquid domain, the connected components of the gas domain (bubbles), the pressure  $P$  in the gas domain and the curvature  $\kappa$  (and the normal vector  $\mathbf{n}$ ) on the liquid-gas interface. These unknowns satisfy equations (1), (2), (3) and (4) with the boundary condition (5) on the free surface  $\Gamma_t$ .

### 3 Time Splitting Algorithm

Let  $0 = t^0 < t^1 < t^2 < \dots < t^N = T$  be a subdivision of the time interval  $[0, T]$  and  $\tau^n = t^{n+1} - t^n$  the  $n$ th time step,  $n = 0, 1, 2, \dots, N$ ,  $\tau$  the largest time step.

Let  $\varphi^n$ ,  $\mathbf{v}^n$ ,  $\Omega^n$ ,  $k^n$ ,  $P_i^n$ ,  $B_i^n$ ,  $i = 1, 2, \dots, k^n$  and  $\kappa^n$ ,  $\mathbf{n}^n$  be approximations of  $\varphi$ ,  $\mathbf{v}$ ,  $\Omega$ ,  $k$ ,  $P_i$ ,  $B_i$ ,  $i = 1, 2, \dots, k$  and  $\kappa$ ,  $\mathbf{n}$  respectively at time  $t^n$ . Then the approximations  $\varphi^{n+1}$ ,  $\mathbf{v}^{n+1}$ ,  $\Omega^{n+1}$ ,  $k^{n+1}$ ,  $P_i^{n+1}$ ,  $B_i^{n+1}$ ,  $i = 1, 2, \dots, k^{n+1}$  and  $\kappa^{n+1}$ ,  $\mathbf{n}^{n+1}$  at time  $t^{n+1}$  are computed by means of an implicit splitting algorithm, as illustrated in Figure 3.

First two advection problems are solved, leading to a prediction of the new velocity  $\mathbf{v}^{n+1/2}$  together with the new approximation of the characteristic function of the liquid domain  $\varphi^{n+1}$ . This allows to determine the new liquid domain  $\Omega^{n+1}$ , the new gas domain  $\Lambda \setminus \Omega^{n+1}$  and the new liquid-gas interface  $\Gamma^{n+1}$ . Then the connected components of gas (bubbles)  $B_i^{n+1}$ ,  $i = 1, \dots, k^{n+1}$  are tracked with a procedure we sketch in the following and the constant pressure  $P_i^{n+1}$  in each bubble  $B_i^{n+1}$  is computed. Then an approximation of the curvature  $\kappa^{n+1}$  is obtained on the interface  $\Gamma^{n+1}$  together with the normal vector  $\mathbf{n}^{n+1}$ . Finally, a generalized Stokes problem is solved on  $\Omega^{n+1}$  with boundary condition (5) on  $\Gamma^{n+1}$  and Dirichlet or slip conditions on the boundary of the cavity  $\Lambda$  and the correction of the velocity  $\mathbf{v}^{n+1}$  and the pressure  $p^{n+1}$  in the liquid

are obtained.

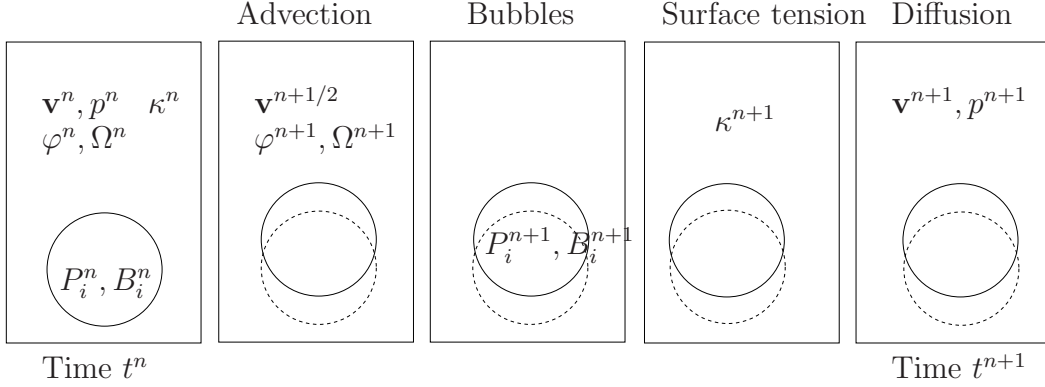


Fig. 3. The splitting algorithm (from left to right). Two advection problems are solved to determine the new approximation of the characteristic function  $\varphi^{n+1}$ , the new liquid domain  $\Omega^{n+1}$  and the predicted velocity  $\mathbf{v}^{n+1/2}$ . Then a constant pressure  $P_i^{n+1}$  is computed in each bubble  $B_i^{n+1}$ . The curvature  $\kappa^{n+1}$  and the normal vector  $\mathbf{n}^{n+1}$  are then obtained on the liquid-gas interface. Finally, a generalized Stokes problem is solved to obtain the velocity  $\mathbf{v}^{n+1}$  and the pressure  $p^{n+1}$  in the new liquid domain  $\Omega^{n+1}$ , taking into account the pressure  $P_i^{n+1}$  and curvature  $\kappa^{n+1}$  on the liquid-gas interface.

The advection step consists in solving between the times  $t^n$  and  $t^{n+1}$  the two advection problems:

$$\frac{\partial \mathbf{v}}{\partial t} + (\mathbf{v} \cdot \nabla) \mathbf{v} = 0, \quad (6)$$

$$\frac{\partial \varphi}{\partial t} + \mathbf{v} \cdot \nabla \varphi = 0, \quad (7)$$

with initial conditions given by the values of the functions  $\mathbf{v}$  and  $\varphi$  at time  $t^n$ . This step is solved with a forward characteristics method, *i.e.* the prediction of the velocity and the new approximation of the characteristic function are given by  $\mathbf{v}^{n+1/2}(x + \tau^n \mathbf{v}^n(x)) = \mathbf{v}^n(x)$  and  $\varphi^{n+1}(x + \tau^n \mathbf{v}^n(x)) = \varphi^n(x)$ , for all  $x \in \Omega^n$ . The domain  $\Omega^{n+1}$  is then defined as the set of points such that  $\varphi^{n+1}$  equals one.

Given the liquid domain  $\Omega^{n+1}$ , the bubbles of gas  $B_i^{n+1}$  are then recognized with a numbering algorithm. The key point is to find the bubbles number  $k^{n+1}$  and the bubbles  $B_i^{n+1}$ ,  $i = 1, \dots, k^{n+1}$ . The algorithm for detecting a connected component of the gas domain is the following. At each time step, given a point  $P$  outside the liquid domain  $\overline{\Omega^{n+1}}$ , we first search for a function  $u$  such that  $-\Delta u = \delta_P$  in the domain  $\Theta^{n+1}$  initially defined by  $\Lambda \setminus \overline{\Omega^{n+1}}$ , with  $u = 0$  on  $\Lambda \setminus \Theta^{n+1}$  and  $u$  continuous, *i.e.*: find  $u : \Lambda \rightarrow \mathbb{R}$  which satisfies:

$$\begin{cases} -\Delta u = \delta_P, & \text{in } \Theta^{n+1}, \\ u = 0, & \text{in } \Lambda \setminus \Theta^{n+1}, \\ [u] = 0, & \text{on } \partial\Theta^{n+1}, \end{cases} \quad (8)$$

where  $\delta_P$  is the Dirac mass centered in  $P$ . Since the solution  $u$  to this problem is strictly positive in the connected component of  $\Theta^{n+1}$  containing the point  $P$  and is vanishing outside, the first bubble is found. The procedure is then repeated to recognize one connected component after the other by removing the previous connected component from  $\Theta^{n+1}$  and choosing another point  $P$ . Details may be found in [5].

Then the curvature of the free surface  $\Gamma^{n+1}$  and the normal vector  $\mathbf{n}^{n+1}$  are computed. Details may be found in [4]. Since the characteristic function  $\varphi^{n+1}$  is not regular across the interface, it is first smoothed by convolution in order to obtain a smooth function  $\tilde{\varphi}^{n+1}$ .

The smoothing by convolution is achieved with a *kernel* function [3, 4] and is given by:

$$\tilde{\varphi}^{n+1}(x) = \int_{\Lambda} \varphi^{n+1}(y) K_{\varepsilon}(x - y) dy, \quad \forall x \in \Lambda. \quad (9)$$

At each time step, the liquid-gas interface is therefore given by the contour line  $\{x \in \Lambda : \tilde{\varphi}^{n+1}(x) = 1/2\}$  (with  $\tilde{\varphi}^{n+1} < 1/2$  in the gas domain and  $\tilde{\varphi}^{n+1} > 1/2$  in the liquid domain); Moreover, the normal vector  $\mathbf{n}^{n+1}$  directed outside the liquid domain towards the gas domain and the curvature  $\kappa^{n+1}$  on the liquid-gas interface are given by:

$$\mathbf{n}^{n+1} = -\frac{\nabla \tilde{\varphi}^{n+1}}{\|\nabla \tilde{\varphi}^{n+1}\|}, \quad \kappa^{n+1} = \nabla \cdot \mathbf{n}^{n+1} = -\nabla \cdot \frac{\nabla \tilde{\varphi}^{n+1}}{\|\nabla \tilde{\varphi}^{n+1}\|}, \quad (10)$$

where  $\|\cdot\|$  denotes the Euclidean norm in  $\mathbb{R}^d$ ,  $d = 2, 3$ .

**Remark 1** *Observe that the first derivatives of  $\tilde{\varphi}^{n+1}$  may even be obtained with an exact expression:*

$$\frac{\partial \tilde{\varphi}^{n+1}}{\partial x_i}(x) = \int_{\Lambda} \varphi^{n+1}(y) \frac{\partial K_{\varepsilon}}{\partial x_i}(x - y) dy, \quad i = 1, \dots, d.$$

where  $d = 2, 3$  is the space dimension of the problem.

Finally, the diffusion step consists in solving a generalized Stokes problem on the domain  $\Omega^{n+1}$  using the predicted velocity  $\mathbf{v}^{n+1/2}$  and the boundary condition (5). The following implicit Euler scheme is used:

$$\rho \frac{\mathbf{v}^{n+1} - \mathbf{v}^{n+1/2}}{\tau^n} - 2\nabla \cdot (\mu \mathbf{D}(\mathbf{v}^{n+1})) + \nabla p^{n+1} = \mathbf{f} \quad \text{in } \Omega^{n+1}, \quad (11)$$

$$\nabla \cdot \mathbf{v}^{n+1} = 0 \quad \text{in } \Omega^{n+1}. \quad (12)$$

The boundary conditions on the free surface between the liquid and the bubble number  $i$  are given by (5). The weak formulation corresponding to (11) (12) and (5) therefore consists in finding  $\mathbf{v}^{n+1}$  and  $p^{n+1}$  such that  $\mathbf{v}^{n+1}$  satisfies the essential boundary conditions on the boundary of the cavity  $\Lambda$  and

$$\begin{aligned} & \int_{\Omega^{n+1}} \frac{\mathbf{v}^{n+1} - \mathbf{v}^{n+1/2}}{\tau^n} \mathbf{w} dx + 2\mu \int_{\Omega^{n+1}} D(\mathbf{v}^{n+1}) : D(\mathbf{w}) dx \\ & - \int_{\Omega^{n+1}} p^{n+1} \nabla \cdot \mathbf{w} dx - \int_{\Omega^{n+1}} \mathbf{f} \mathbf{w} dx - \int_{\Omega^{n+1}} \nabla \cdot \mathbf{v}^{n+1} q dx \\ & + \int_{\Gamma^{n+1}} (P^{n+1} - \sigma \kappa^{n+1}) \mathbf{n}^{n+1} \mathbf{w} dS = 0, \end{aligned} \quad (13)$$

for all  $(\mathbf{w}, q)$  compatible with the essential boundary conditions on the boundary of  $\Omega^{n+1}$ .

#### 4 Two-Grids Method for Space Discretization

A two-grids method is used for the spatial discretization, see Figure 4. In particular, a regular grid of small cells is used to solve the advection step, while the computations of the gas pressure, surface tension effects and diffusion step are performed on an unstructured finite element mesh.

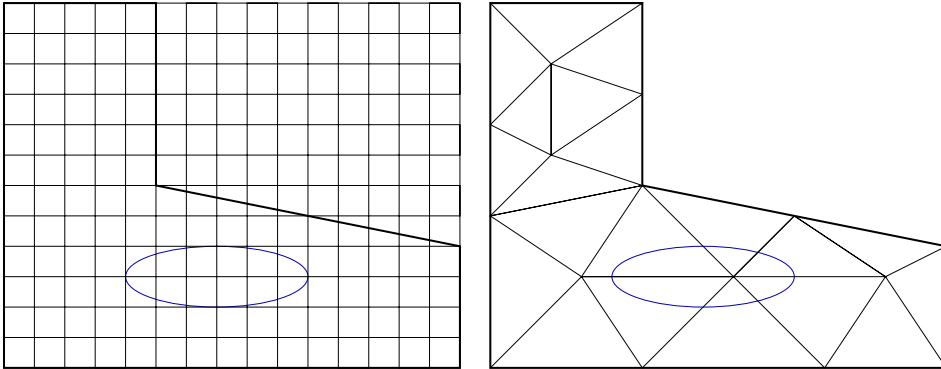


Fig. 4. Two grids method in the two-dimensional case: structured grid of small square cells (left) and unstructured finite element mesh of triangles (right).

The advection step is solved on the fine structured grid of small cells with a forward characteristics method. Assume that the grid is made out of cubic cells of size  $h$  ( $d = 3$ ), each cell being labeled by indices  $(ijk)$ . Let  $\varphi_{ijk}^n$  and  $\mathbf{v}_{ijk}^n$  be the approximate value of  $\varphi$  and  $\mathbf{v}$  at the center of cell number  $(ijk)$

at time  $t^n$ . The unknown  $\varphi_{ijk}^n$  is the so-called volume fraction of liquid in the cell  $(ijk)$ , see [1]. This numerical approximation of the characteristic function  $\varphi$  at time  $t^n$  is then piecewise constant on each cell of the structured grid. The advection step in the cell  $(ijk)$  consists in advecting  $\varphi_{ijk}^n$  and  $\mathbf{v}_{ijk}^n$  by  $\tau^n \mathbf{v}_{ijk}^n$  and then projecting the values on the structured grid. An example of cell advection and projection is presented in Figure 5 in two space dimensions.

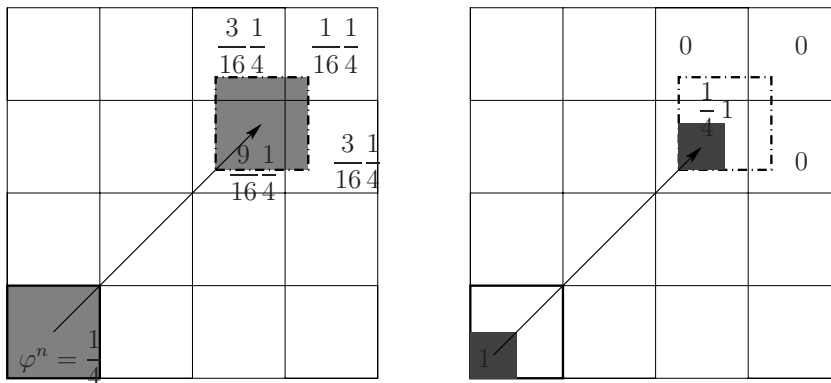


Fig. 5. An example of two dimensional advection of  $\varphi_{ij}^n$  by  $\tau^{n+1} \mathbf{v}_{ij}^n$ , and projection on the grid. The advected cell is represented by the dashed lines. The four cells containing the advected cell receive a fraction of  $\varphi_{ij}^n$ , according to the position of the advected cell.

In order to enhance the quality of the volume fraction of liquid, post-processing procedures have been implemented. In particular, a variation of the SLIC algorithm [16] allows to reduce the numerical diffusion on the regular grid of small cells by pushing the liquid on the sides of the cell before advecting it and projecting on the grid. Precise examples and detailed description are given in [13, 14] for the two- and three-dimensional cases. A post-processing technique which allows to produce new values  $\varphi_{ijk}^{n+1}$  which are between zero and one is also implemented (see [13, 14] for details).

Once values  $\varphi_{ijk}^{n+1}$  and  $\mathbf{v}_{ijk}^{n+1/2}$  have been computed on the cells, values of the fraction of liquid  $\varphi_P^{n+1}$  and of the velocity field  $\mathbf{v}_P^{n+1/2}$  are computed at the nodes  $P$  of the finite element mesh by two-grids restriction methods: for any vertex  $P$  of the finite element mesh let  $\psi_P$  be the corresponding basis function (i.e. the continuous, piecewise affine, 'hat' function having value one at  $P$ , zero at the other vertices of the finite element mesh). We consider all the tetrahedrons  $K$  containing vertex  $P$  and all the cells  $(ijk)$  having center of mass  $C_{ijk}$  contained in these tetrahedrons. Then,  $\varphi_P^{n+1}$ , the volume fraction of liquid at vertex  $P$  and time  $t^{n+1}$  is computed using the following weighted sum:

$$\varphi_P^{n+1} = \frac{\sum_{P \in K} \sum_{\substack{ijk \\ C_{ijk} \in K}} \psi_P(C_{ijk}) \varphi_{ijk}^{n+1}}{\sum_{P \in K} \sum_{\substack{ijk \\ C_{ijk} \in K}} \psi_P(C_{ijk})}.$$

The same kind of formula is used to obtain the predicted velocity  $\mathbf{v}^{n+1/2}$  at the vertices of the finite element mesh. When these values are available at the vertices of the finite element mesh, the liquid region is defined as follows. An element of the finite element mesh is said to be liquid if (at least) one of its vertices  $P$  has a value  $\varphi_P^{n+1} > 0.5$ . The computational domain used for solving (13) is then defined to be the union of all liquid elements.

The numbering of the bubbles of gas requires to solving Poisson problems (8). The Poisson problems are solved on the finite element unstructured mesh, using piecewise linear finite elements. Once the connected components of the gas domain are recognized, a constant pressure is computed by using the law of ideal gases (4). The volume of each bubble of gas is computed by the sum of the volumes of the elements of the finite element mesh belonging to the bubble, weighted by the mean volume fraction of liquid. Details may be found in [5].

Several methods for the computation of an approximation of the curvature may be found in the literature (see *e.g.* [1, 20, 21]). We use here a formulation on the finite element unstructured mesh.

Let  $\mathcal{T}_h$  be the triangulation of the cavity  $\Lambda$ ,  $\Omega_h^{n+1}$  be the approximation of the liquid domain composed by elements  $K$  in  $\mathcal{T}_h$  and  $\Gamma_h^{n+1}$  the approximation of  $\Gamma^{n+1}$ . Let  $\psi_{P_j}$  be the basis functions of the piecewise affine finite element space associated to each node  $P_j$ ,  $j = 1, \dots, N$  in the cavity. Finally, let the piecewise affine finite elements space be denoted by  $X_h^1(\Lambda)$ .

Let  $\tilde{\varphi}_h^{n+1}$  be the approximation of  $\tilde{\varphi}^{n+1}$  in  $X_h^1(\Lambda)$ . The numerical integration of (9), performed on the finite element mesh, leads to an approximation of the smoothed volume fraction of liquid  $\tilde{\varphi}_h^{n+1}$  for each grid point  $P_i$  of  $\mathcal{T}_h$ .

The normal vector  $\mathbf{n}_h^{n+1}$  is given by (10) (with  $\varphi^{n+1}$  replaced by  $\varphi_h^{n+1}$ ) at each grid point  $P_j$ . The approximation of the curvature  $\kappa^{n+1}$  in (10) is denoted by  $\kappa_h^{n+1}$ . It is computed by the  $L^2$ -projection of the divergence of the normal vector on the piecewise linear finite elements space:

$$\int_{\Lambda} \kappa_h^{n+1} \psi_P dx = \int_{\Lambda} -\nabla \cdot \frac{\nabla \tilde{\varphi}_h^{n+1}}{\|\nabla \tilde{\varphi}_h^{n+1}\|} \psi_P dx, \quad (14)$$

for all vertices  $P$  of  $\mathcal{T}_h$ . The left-hand side of this relation is computed with *mass lumping*, while the right-hand side is integrated by parts. This leads to:

$$\begin{aligned} \kappa_h^{n+1}(P_j) = \frac{d+1}{|\Omega_j|} & \left[ \sum_{K \in \mathcal{T}_h} |K| \left( \frac{1}{d+1} \sum_{P_i \in K} \frac{\nabla \tilde{\varphi}_h^{n+1}(P_i)}{\|\nabla \tilde{\varphi}_h^{n+1}\|} \right) \nabla \psi_{P_j} \Big|_K \right. \\ & \left. - \sum_{\substack{\partial K \subset \partial \Lambda \\ P_j \in K}} \frac{1}{d} \frac{\nabla \tilde{\varphi}_h^{n+1}(P_j)}{\|\nabla \tilde{\varphi}_h^{n+1}\|} \mathbf{n}_{\Lambda, h}(P_j) |\partial K| \right], \end{aligned} \quad (15)$$

where  $|\Omega_j| = \sum_{K, P_j \in K} |K|$  and  $\mathbf{n}_{\Lambda, h}$  denotes the approximation of the external normal vector to the cavity  $\Lambda$ .

Explicit values of the curvature of the level lines of  $\tilde{\varphi}_h^{n+1}$  are obtained at the vertices of the finite element mesh located in a layer around the free surface. The restriction of  $\kappa_h^{n+1}$  to the nodes lying on the interface  $\Gamma_h^{n+1}$  is used to compute (5).

Finally the diffusion step consists in solving the Stokes problem (13). Let  $\mathbf{v}_h^{n+1}$  (resp.  $p_h^{n+1}$ ) be the piecewise linear approximation of  $\mathbf{v}^{n+1}$  (resp.  $p^{n+1}$ ). The Stokes problem is solved with stabilized  $\mathbb{P}_1 - \mathbb{P}_1$  finite elements (Galerkin Least Squares method) and consists in finding the velocity  $\mathbf{v}_h^{n+1}$  and pressure  $p_h^{n+1}$  such that:

$$\begin{aligned} & \int_{\Omega_h^{n+1}} \frac{\mathbf{v}_h^{n+1} - \mathbf{v}_h^{n+1/2}}{\tau^n} \mathbf{w} dx + 2\mu \int_{\Omega_h^{n+1}} \mathbf{D}(\mathbf{v}_h^{n+1}) : \mathbf{D}(\mathbf{w}) dx - \int_{\Omega_h^{n+1}} \mathbf{f} \mathbf{w} dx \\ & - \int_{\Omega_h^{n+1}} p_h^{n+1} \nabla \cdot \mathbf{w} dx + \int_{\Gamma_h^{n+1}} (P^{n+1} - \sigma \kappa_h^{n+1}) \mathbf{n}_h^{n+1} \mathbf{w} dS - \int_{\Omega_h^{n+1}} \nabla \cdot \mathbf{v}_h^{n+1} q dx \\ & - \sum_{K \subset \Omega_h^{n+1}} \alpha_K \int_K \left( \frac{\mathbf{v}_h^{n+1} - \mathbf{v}_h^{n+1/2}}{\tau^n} + \nabla p_h^{n+1} - \mathbf{f} \right) \cdot \nabla q dx = 0, \end{aligned} \quad (16)$$

for all  $\mathbf{w}$  and  $q$  the velocity and pressure test functions, compatible with the boundary conditions on  $\partial \Lambda$ . Following [13, 14], the value of the parameter  $\alpha_K$  is given by

$$\alpha_K = \begin{cases} \frac{1}{12} \frac{h_K^2}{\mu}, & \text{if } Re_K \leq 3, \\ \frac{1}{4 Re_K} \frac{h_K^2}{\mu}, & \text{otherwise,} \end{cases} \quad (17)$$

where  $h_K$  is the diameter of the element  $K$  and  $Re_K$  is the local Reynolds number, defined as  $Re_K = \frac{\rho h_K \max_{\mathbf{x} \in K} |\mathbf{v}_h^{n+1/2}(\mathbf{x})|}{2\mu}$ .

The restriction of the continuous piecewise linear approximation of the velocity  $\mathbf{v}_h^{n+1}$  at the center of each cells  $C_{ijk}$  permits to obtain the values  $\mathbf{v}_{ijk}^{n+1}$  on the structured grid for the next time step as follows:

$$\mathbf{v}_{ijk}^{n+1} = \sum_{P \in K} \mathbf{v}_P^{n+1} \psi_P(C_{ijk}).$$

## 5 Numerical Results in Two Dimensions

Following [22, 23], where a two-dimensional view of bubbles rising under an inclined plane are experimentally considered, we first tackle the two-dimensional case. The numerical setup is detailed in the following. The numerical simulations are first undertaken for a gas bubble (zero density) in water ( $\rho = 1000 \text{ kg/m}^3$ ,  $\mu = 0.001 \text{ kg/(m s)}$ ,  $\sigma = 0.0728 \text{ N/m}$ ) in order to compare with the experiments mentioned earlier. A comparison with a gas bubble in alumina-cryolite bath ( $\rho = 2150 \text{ kg/m}^3$ ,  $\mu = 0.0015 \text{ kg/(m s)}$ ,  $\sigma = 0.01 \text{ N/m}$ ) is discussed.

### 5.1 Numerical Setup

Let us consider one aluminum cell with two anodes. Large bubbles are located under the anodes. When enforcing a positive slope for the bottom of the anode, one can force the bubble to escape on the outer side of the cell, as illustrated in Figure 6. Under gravity forces, the bubble is escaping from under the anode and arises in the canal next to the anode. We consider two inclined anodes with (opposite) angle  $\alpha$ . The bubbles therefore escape at the extremities of the domain. The dimension of the domain are  $H \times L = 2.4 \times 0.6 \text{ [m]}$ , corresponds to a transverse cut of the three-dimensional domain, similar to the one under the camera angle in [22]. One large bubble is initially placed under one anode. Unlike in the experimental results, there is no nucleation model for bubbles formation in the simulation framework. Under buoyancy effects, the bubble escapes from under the anode and rises in the canal next to the anode. Gas in the bubbles can escape at the top of the domain.

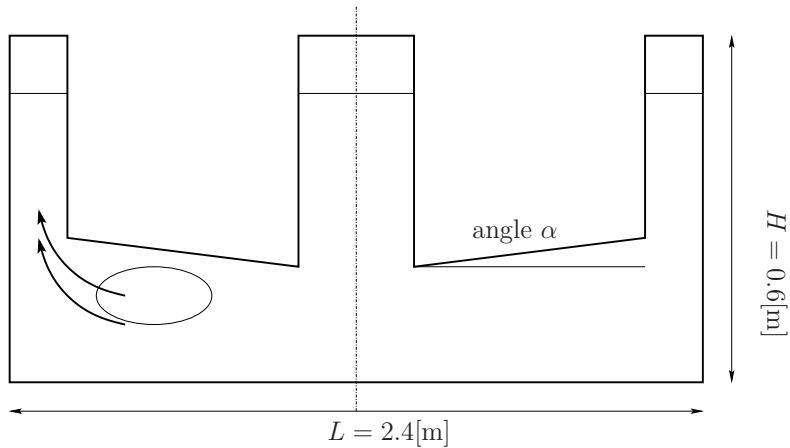


Fig. 6. Setup of the aluminum cell. The liquid flow is located under two inclined anodes. Large bubbles initially located under the anode escape into the canal next to the anode.

By symmetry, we are interested here only in one-half of the domain. One typical example of the regular mesh created with MODULEF [2] is illustrated in Figure 7.

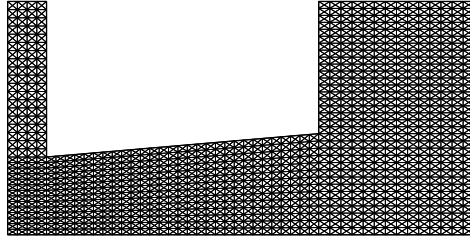


Fig. 7. Coarse mesh for the triangulation of (one half of) the aluminum cell.

### 5.2 Formation of the Fortin 'Head and Tail' Bubble

When escaping from under the inclined plane symbolizing the anode, the dynamics effects of the flow give the bubble a particular shape, called the *Fortin shape* or *head and tail* shape, as first documented in [8]. The Fortin shape for a two-dimensional bubble consists of an asymmetric 'head and tail' shape that is represented in Figure 8 (extracted from [22]).

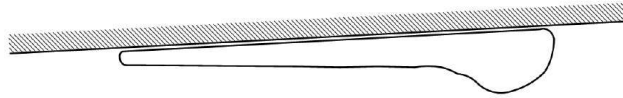


Fig. 8. Fortin 'head and tail' shape for a large bubble under an inclined plane (from [22]).

We consider first a two-dimensional coarse mesh; typically the size of the finite elements is approx.  $H = 0.0081482$ , and the size of the cells is approx.  $h = 0.002$ . A numerical simulation for a large bubble (with initial volume of  $0.0113 \text{ m}^2$ ) that incorporates the pressure in the compressible gas but neglects the surface tension effects allows to reproduce such a shape. Figure 9 visualizes the interface of the bubble under the anode; it typically matches the Fortin shape observed experimentally.

### 5.3 Escape and Break-up of a Single Large Bubble

Classical results for rising bubbles describe the shape, volume and curvature of the bubble (see for instance [4, 11] and reference therein). When considering a bubble under an inclined plane, the time evolution of the bubble shape is much different. Experiments have been described in [12, 15, 22] for instance. Typically, the bubble first takes the shape of a Fortin bubble under the anode;

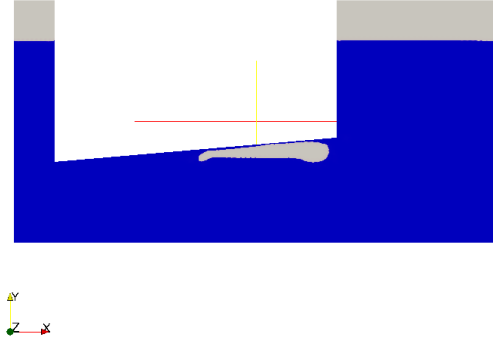


Fig. 9. Fortin 'head and tail' shape for a large bubble under an inclined plane: simulation result with  $H = 0.0081482$ , gas pressure in the bubble, no surface tension effects.

then escapes in the vertical canal. When escaping, the bubble breaks into two distinct pieces: one piece rises, while the other remains trapped under the anodes, and moves in the other direction due to the *back-flow* under the anode provoked by the first bubble.

Figures 10 and 11 illustrate the evolution of the bubbles for a coarse ( $H = 0.0081482$ ) and fine mesh ( $H = 0.0038479$ ) respectively. The pressure in the gas is taken into account, but the surface tension effects are neglected. The initial bubble is given by the ellipse shape:

$$\Lambda \setminus \Omega = \left\{ \frac{(x - 0.6)^2}{16} + (y - 0.2)^2 \leq 0.03^2 \right\}.$$

and the fluid is initially at rest. The initial pressure in the bubble is given by  $P = 105'300$  [atm] (which corresponds to the sum of the atmospheric pressure at the surface and the pressure added by the column of water over the bubble). The body forces are given by  $\mathbf{F} = \rho \mathbf{g}$ , with  $\mathbf{g} = (0, -9.81)^T$  m/s<sup>2</sup>. We perform 1000 time steps of size  $\tau = 0.005$  s. on the coarse mesh, and 2000 time steps of size  $\tau = 0.001$  s. on the fine mesh.

We can observe a couple features numerically that are also observed from the experimental point of view:

- Very clearly, the largest the bubble, the faster the displacement of the bubble. This is confirmed by the fact that the small bubble that is trapped under the anode after the break-up of the large one is relatively static.
- The formation of the Fortin head and tail shape is due to dynamical effects;

more precisely, if the anode is horizontal, this shape is not produced as the bubble is statically trapped under the anode. When the volume of the bubble is large enough, the flow under the anode provokes the formation of this particular shape. This phenomenon is reproduced for any (reasonable) grid resolution.

- The break-up and escape of the bubbles induces a *back-flow* effect under the anode.
- The break-up of the bubble into a large rising bubble, and a smaller bubble that remains trapped under the anode can be reproduced only with meshes that are fine enough.

#### 5.4 Influence of the Inclined Angle

The influence of the angle of the anode has been discussed from the experimental point of view in [12, 15]. Simulation results for various angles between 2 and 10 degrees are presented in Figure 12. As in the experiments, the bubble escape faster when the angle is wider. From the numerical point of view, the bubble remains stuck under the anode, if the angle is not wide enough to counterbalance numerical viscosity forces. In Figure 12, we emphasize that the break-up does not occur (at least no in a reasonable time) when the angle is only 2 degrees.

#### 5.5 Comparison Water-Aluminum

Figure 13 illustrates the evolution of a single large bubble of gas evolving in the aluminum-cryolite solution ( $\rho = 2150 \text{ kg/m}^3$ ,  $\mu = 0.0015 \text{ kg/(m s)}$ ). We observe that the changes in the physical parameters of the fluid do not change drastically the evolution of the bubble, which justifies the use of gas bubbles in water in the experimental setup.

#### 5.6 Influence of Surface Tension Effects

Finally let us consider the simulation of a gas bubble in water, with the fine mesh ( $H = 0.0038479$ ), while adding the surface tension effects ( $\sigma = 0.0728 \text{ N/m}$ ). Figure 14 illustrates a comparison of the simulation with and without surface tension effects. One can observe that the formation of small secondary bubbles are slightly reduced, but the general evolution of the bubble remains similar, as expected for large bubbles.

## 6 Numerical Results in Three Dimensions

### 6.1 Numerical Setup

In a similar fashion, let us consider the three-dimensional case. We consider two inclined anodes with (opposite) angles  $\alpha$ . The bubbles therefore escape at the extremities of the domain. The dimension of the domain are  $H \times L \times D = 2.4 \times 0.6 \times 0.5$  [m], as illustrated in Figure 15. By symmetry, we are interested here only in one-half of the domain. A regular mesh is created with MODULEF [2] by extrusion of the two-dimensional mesh illustrated in Figure 7.

### 6.2 Escape and Break-Up of a Single Large Bubble

One large bubble is initially placed under one anode, with elliptic shape:

$$\Lambda \setminus \Omega = \left\{ \frac{(x - 0.6)^2}{16} + (y - 0.2)^2 + (z - 0.25)^2 \leq 0.07^2 \right\}.$$

and the fluid is initially at rest. The initial pressure in the bubble is given by  $P = 105'300$  [atm]. The body forces are given by  $\mathbf{F} = -\rho\mathbf{g}$ , with  $\mathbf{g} = (0, -9.81)^T$  m/s<sup>2</sup>. The regular three-dimensional mesh consists of 33600 grid points and 180000 tetrahedra, whose typical size is given by  $H = 0.033$ . The size of the grid cells is  $h = 3 \cdot 10^{-3}$ . We perform 500 time steps of size  $\tau = 0.005$  s., and neglect the surface tension effects. Snapshots of the numerical results are visualized in Figure 16.

## 7 Conclusions

A numerical framework for the simulation of large bubbles has been presented. The particular application to large bubbles rising under an anode in the aluminum electrolysis has been detailed. Numerical experiments agree with experiments, as i) they show the formation of Fortin bubbles; ii) reproduce accurately the break-up and escape of a bubble from under the anode, in two and three space dimensions, and iii) confirm that the surface tension effects are not highly relevant for large bubbles.

## Acknowledgments

This research project is supported by the Rio Tinto - Alcan company. The authors particularly thank the group from *Laboratoire de Recherche et Fabrication* in Saint-Jean de Maurienne, France, for fruitful discussions. The first author gratefully acknowledges the support of the Institute of Analysis and Scientific Computing (EPFL): this work has been partially achieved during his sabbatical leave in 2009-2010 at EPFL.

## References

- [1] E. Aulisa, S. Manservigi, and R. Scardovelli. A mixed markers and volume-of-fluid method for the reconstruction and advection of interfaces in two-phase and free-boundary flows. *J. Comp. Phys.*, 188:611–639, 2003.
- [2] M. Bernadou, P.L. George, A. Hassim, P. Joly, P. Laug, A. Perronet, E. Saltel, D. Steer, G. Vanderborck, and M. Vidrascu. Modulef, a modular library of finite elements. Technical report, INRIA, 1988.
- [3] J. U. Brackbill, D. B. Kothe, and C. Zemach. A continuum method for modeling surface tension. *J. Comp. Phys.*, 100:335–354, 1992.
- [4] A. Caboussat. A numerical method for the simulation of free surface flows with surface tension. *Computers and Fluids*, 35(10):1205–1216, 2006.
- [5] A. Caboussat, M. Picasso, and J. Rappaz. Numerical simulation of free surface incompressible liquid flows surrounded by compressible gas. *J. Comput. Phys.*, 203(2):626–649, 2005.
- [6] M. Flück, T. Hofer, M. Picasso, J. Rappaz, and G. Steiner. Scientific computing for aluminum production. *Int. J. Numer. Anal. and Modeling*, 6(3):489–504, 2009.
- [7] M. Flück, A. Janka, C. Laurent, M. Picasso, J. Rappaz, and G. Steiner. Some mathematical and numerical aspects in aluminum production. *J. Sci. Comp.*, Online first, 2008.
- [8] S. Fortin, M. Gerhardt, and J. A. Gesing. Physicall modelling of bubble behaviour and gas release from aluminium reduction cell anodes. *TMS Light Metals*, pages 721–741, 1984.
- [9] L. P. Franca and S. L. Frey. Stabilized finite element method: II. the incompressible Navier-Stokes equations. *Comp. Meth. Appl. Mech. Engrg*, 99:209–233, 1992.
- [10] R. Glowinski. *Finite Element Method For Incompressible Viscous Flow*, volume IX of *Handbook of Numerical Analysis (P.G. Ciarlet, J.L. Lions eds)*, pages 3–1176. Elsevier, Amsterdam, 2003.
- [11] S. Hysing, S. Turek, D. Kuzmin, N. Parolini, E. Burman, S. Ganesan, and L. Tobiska. Quantitative benchmark computations of two-dimensional bubble dynamics. *Int. J. Numer. Meth. Fluids*, 60:1259–1288, 2009.

- [12] C. C. Maneri and N. Zuber. An experimental study of plane bubbles rising at inclination. *Int. J. Multiphase Flow*, 1:623–645, 1974.
- [13] V. Maronnier, M. Picasso, and J. Rappaz. Numerical simulation of free surface flows. *J. Comput. Phys.*, 155:439–455, 1999.
- [14] V. Maronnier, M. Picasso, and J. Rappaz. Numerical simulation of three dimensional free surface flows. *Int. J. Num. Meth. Fluids*, 42(7):697–716, 2003.
- [15] T. Maxworthy. Bubble rise under an inclined plane. *J. Fluid Mech.*, 229:659–674, 1991.
- [16] W.F. Noh and P. Woodward. *SLIC (Simple Line Interface Calculation)*, volume 59 of *Lectures Notes in Physics*, pages 330–340. Springer-Verlag, 1976.
- [17] A. Perron, L. I. Kiss, and S. Poncsák. An experimental investigation of the motion of single bubbles under a slightly inclined surface. *Int. J. Multiphase Flow*, 32:606–622, 2006.
- [18] A. Perron, L. I. Kiss, and S. Poncsák. Mathematical model to evaluate the ohmic resistance caused by the presence of a large number of bubbles in Hall-Héroult cells. *J. Applied Electrochemistry*, 37:303–310, 2007.
- [19] O. Pironneau. *Finite Element Methods for Fluids*. Wiley, Chichester, 1989.
- [20] W.J. Rider and D.B. Kothe. Reconstructing volume tracking. *J. Comp. Phys.*, 141:112–152, 1998.
- [21] R. Scardovelli and S. Zaleski. Direct numerical simulation of free surface and interfacial flows. *Annual Review of Fluid Mechanics*, 31:567–603, 1999.
- [22] K. Vékony and L. I. Kiss. Morphology of two-phase layers with large bubbles. Technical report, Université du Québec à Chicoutimi, 2009.
- [23] K. Vékony and L. I. Kiss. Velocity measurements in a real size model of an aluminium electrolysis cell model using the PIV techniques. Technical report, Université du Québec à Chicoutimi, 2009.

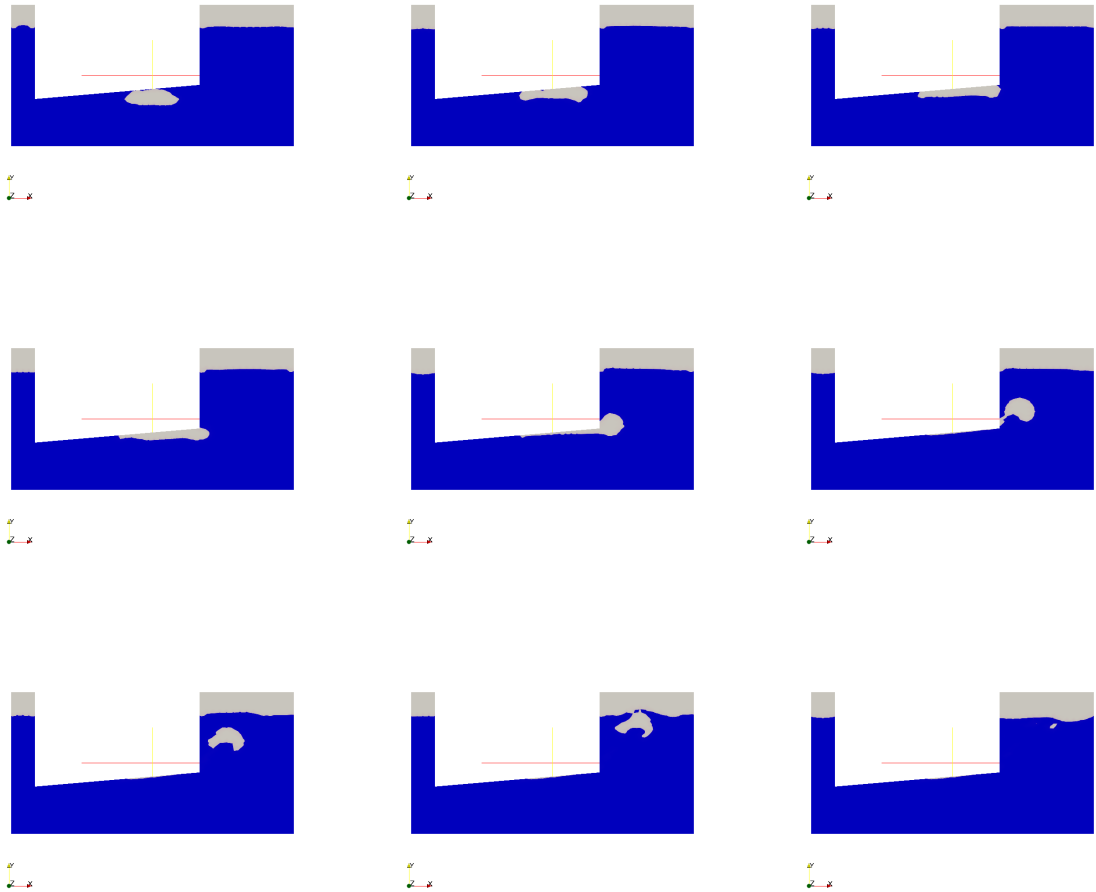


Fig. 10. Numerical simulation of a bubble rising under an inclined plane under gravity forces ( $H = 0.0081482$ ). The angle is equal to  $5^\circ$  degrees. Snapshots of the solution at times  $t = 0.05, 0.5, 1.0, 1.5, 2.0, 2.25, 2.5, 2.75$  and  $3.0$  s. (top to bottom, left to right).

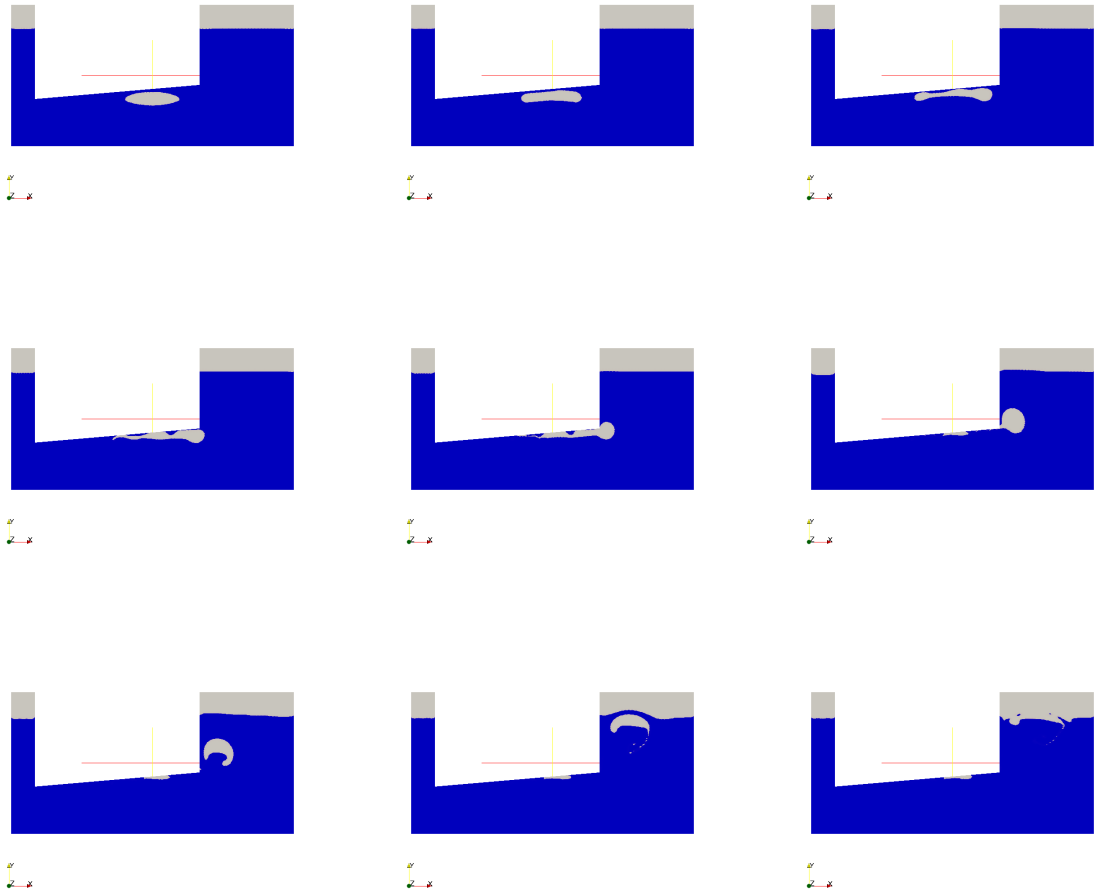
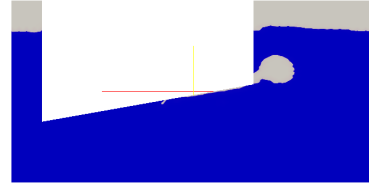
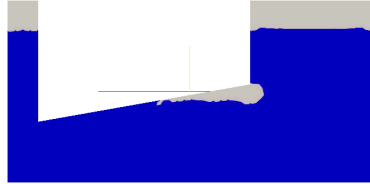


Fig. 11. Numerical simulation of a bubble rising under an inclined plane under gravity forces ( $H = 0.0038479$ ). The angle is equal to  $5^\circ$  degrees. Snapshots of the solution at times  $t = 0.1, 0.5, 1.0, 1.5, 2.0, 2.5, 3.0, 4.0$  and  $4.5$  s. (top to bottom, left to right).

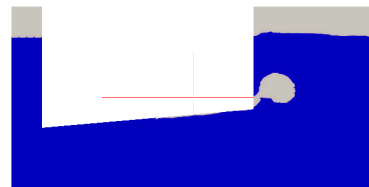
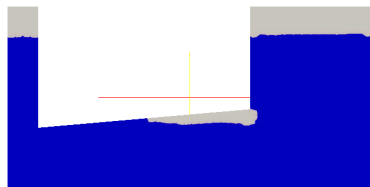
Fortin bubble

Breakup

$\alpha = 10^\circ$



$\alpha = 5^\circ$



$\alpha = 2^\circ$

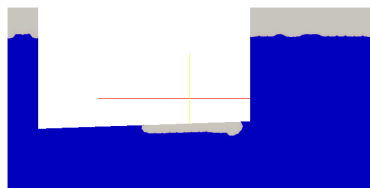


Fig. 12. Numerical simulation of a bubble rising under an inclined plane under gravity forces ( $H = 0.0081482$ ), for  $\alpha = 10, 5$  and  $2$  degrees (top to bottom). Left: formation of the Fortin shape; Right: break-up and escape of the bubble in the vertical canal.

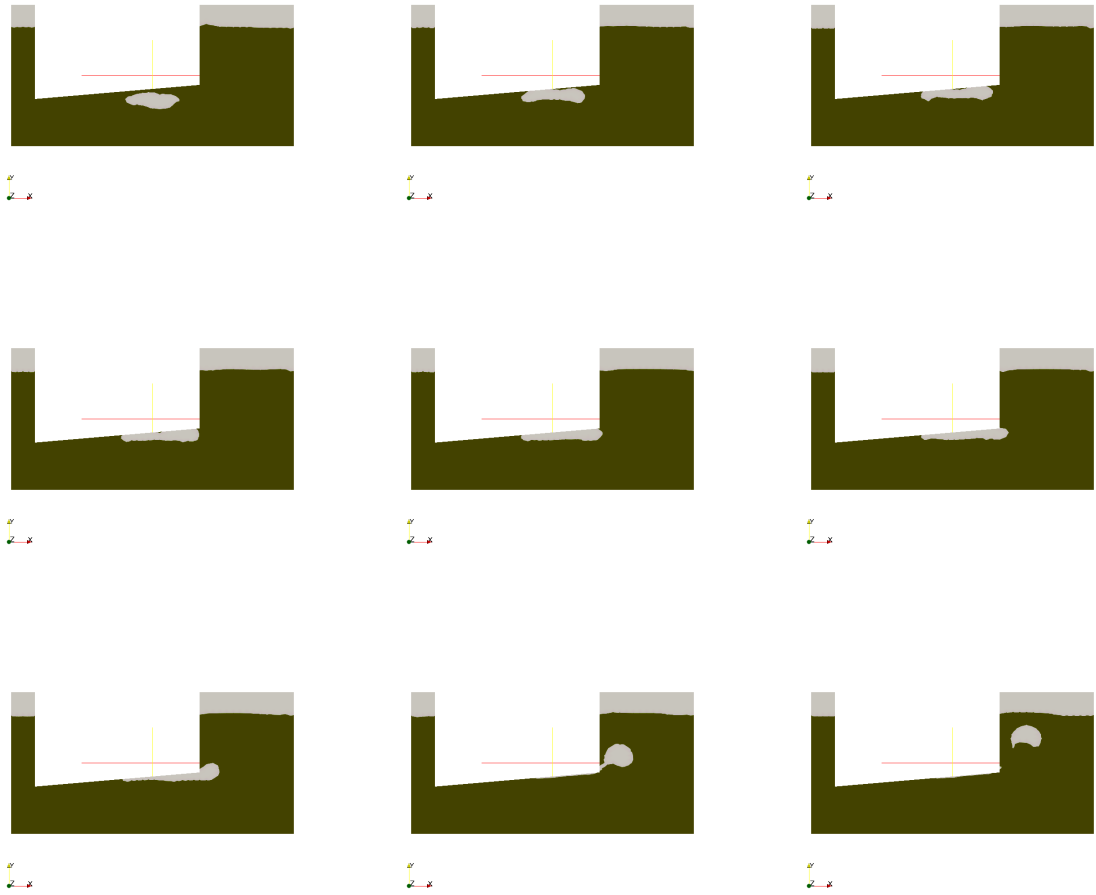


Fig. 13. Numerical simulation of a gas bubble in aluminum-cryolite rising under an inclined plane under gravity forces ( $H = 0.0081482$ ). The angle is equal to  $5^\circ$  degrees. Snapshots of the solution at times  $t = 0.1, 0.5, 1.0, 1.5, 2.0, 2.5, 3.0, 3.5$  and  $4.0$  s. (top to bottom, left to right).

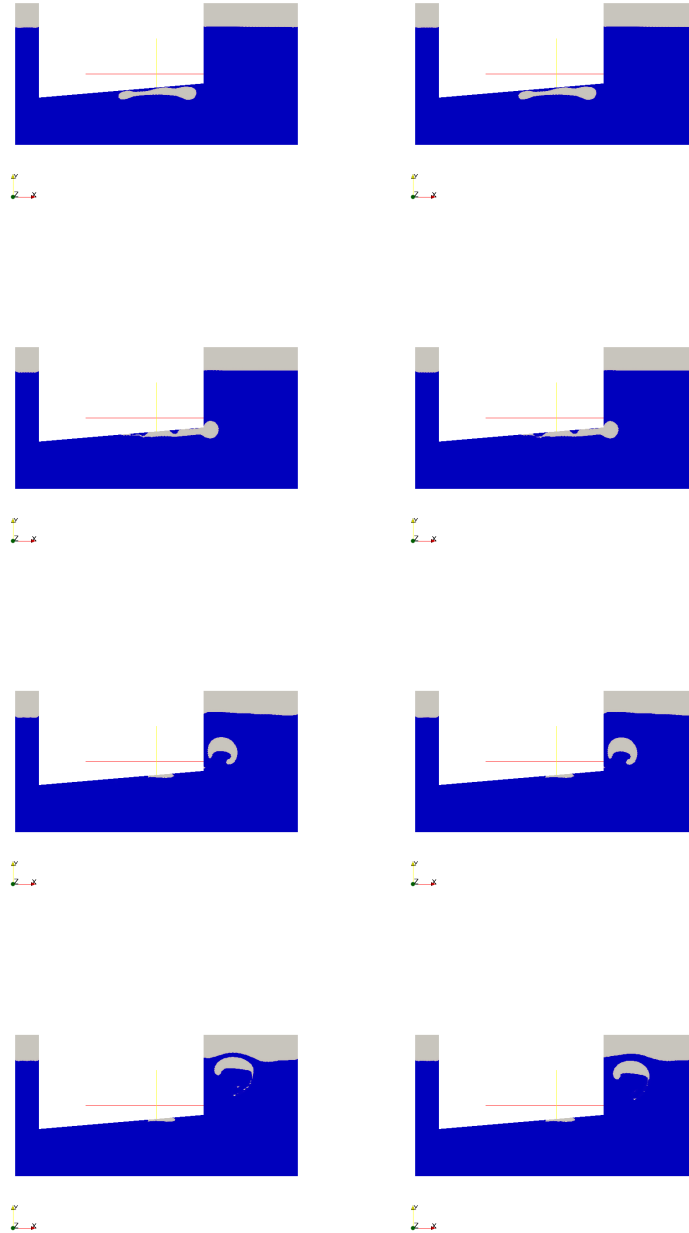


Fig. 14. Numerical simulation of a gas bubble in water rising under an inclined plane under gravity forces ( $H = 0.0038479$ ). The angle is equal to  $5^\circ$  degrees. Snapshot of the solution at times  $t = 1.0, 2.0, 3.0$  and  $4.0$  s. (top to bottom). Left: without surface tension effects ( $\sigma = 0.0$ ); right: with surface tension effects ( $\sigma = 0.0728$ ).

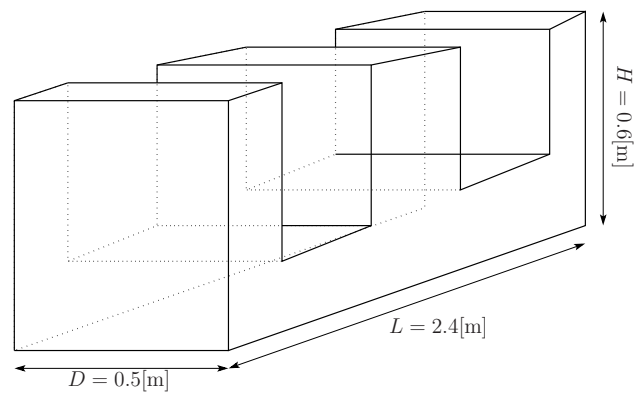


Fig. 15. 3D setup of the aluminum cell. The liquid flow is located under two inclined anodes. Large bubbles initially located under the anode escape into the canal next to the anode.



Fig. 16. Numerical simulation of a bubble rising under an inclined plane under gravity forces ( $H = 0.0333$ ). The angle is equal to  $5^\circ$  degrees. Snapshots of the solution at times  $t = 0.05, 0.5, 1.0, 1.5, 2.0, 2.25, 2.5, 2.75$  and  $3.0$  s. (top to bottom, left to right).